PERGAMON

International Journal of Heat and Mass Transfer 43 (2000) 3589–3606

International Journal of HEAT and MASS TRANSFER

www.elsevier.com/locate/ijhmt

Free surface profiles and thermal convection in electrostatically levitated droplets

S.P. Song, B.Q. Li*

School of Mechanical and Materials Engineering, Washington State University, Pullman, WA 99164, USA

Received 21 August 1998; received in revised form 9 December 1999

Abstract

A numerical analysis is presented of free surface profiles, Marangoni convection and the temperature distribution in electrostatically levitated droplets. The analysis is based on the boundary element solution of electric potential outside the droplet, the weighted residuals formulation of the free surface balance equation involving electrostatic stresses, surface tension and gravity, and the finite element solution of the internal fluid flow and temperature distribution in the electrostatically deformed droplets. Numerical simulations are carried out for several different materials and various operating conditions. Results show that an applied electrostatic field generates a normal stress distribution along the droplet surface, which, combined with surface tension, causes the droplet to deform into an ellipsoidal shape in microgravity and into the shape of a blob with the lower side being flatter under terrestrial conditions. Laser heating induces a non-uniform temperature distribution in the droplet, which in turn produces recirculating convection in the droplet. For the cases studied, Marangoni convection is the predominant mode and buoyancy effects are negligible. It is found that there is a higher temperature gradient and hence stronger Marangoni convection in droplets with higher melting points which require more laser power. The internal recirculating flow may be reduced by more uniform laser heating. During undercooling of the droplet with heating turned off, both temperature and fluid flow fields evolve in time, such that the temperature gradient and the tangential velocities along the droplet surface subside in magnitude and reverse their directions.

1. Introduction

In the upcoming International Space Station, a suite of containerless processing systems will be installed for the fundamental study of nucleation and solidification phenomena and the measurement of thermophysical properties of a wide variety of materials [1–3]. The concept of containerless processing is to levitate a working sample, melt or solid, in air against gravity so that it is free from wall related contamination. In the microgravity environment created in space vehicles, the concept is exploited to confine the sample from drifting in space. Without contact with a solid wall, a levitated droplet can be allowed to cool far below its melting point but still remains liquid, which is called undercooling. With a substantial undercooling, simultaneous nucleation may occur in the melt, followed by grain growth, thereby producing a solid with a microstructure consisting of extremely fine-sized grains. A containerless processing system also offers a uniquely useful means by which the thermophysi-

* Corresponding author.
E-mail address: li@mme.wsu.edu (B.Q. Li).

0017-9310/00/$ - see front matter
PII: S0017-9310(00)00004-1

Nomenclature

a	radius of a sphere
C	geometric coefficient resulting from boundary integral formulation
C_p	heat capacity
E_0	electric field
$E(\kappa)$	elliptical integral of the second kind
$\mathbf{F}$	force vector
$\mathbf{g}$	gravity constant
G	green's function for free space
H	Gaussian curvature
$\mathbf{H}$, $\mathbf{G}$	global coefficient matrices of BE formulation
$\hat{i}$	unit vector of ith component
k	thermal conductivity
$K(\kappa)$	elliptical integral of the first kind
Ma	Marangoni number, $Ma = (\partial\gamma/\partial T)(T_{\min} - T_{\max})a_d\rho C_p/\mu k$
$\mathbf{n}$ (n_r, n_z)	outward normal, its r and z components
P_o	pressure constant
Pr	Prandtl number, $Pr = \mu C_p/k$
Q	net charge on the droplet
Q_c	critical charge
Q_o	laser beam heat flux constant
$\mathbf{r}$, r	point vector and r coordinate in cylindrical coordinates
R	radial coordinate in spherical coordinates with origin at the center of the unformed droplet
Ra	Rayleigh number, $Ra = \rho^2 g C_p \beta a_d^3 (T_{\max} - T_{\min})/\mu k$
Re	Reynolds number, $Re = \rho V_{\max} a_d/\mu$
s	dummy variable for surface integral
$\mathbf{t}$	tangential vector
T, T_∞, T_r	temperature, temperature of surroundings, reference temperature
$T_{\max}$, $T_{\min}$	maximum and minimum temperatures
ΔT	difference between $T_{\max}$ and $T_{\min}$
$V_{\max}$	maximum velocity
$\mathbf{u}$	velocity
$\hat{z}$	unit vector of z-direction
z	z coordinate
z_c	center of mass along the z-axis

Greek symbols

β	thermal expansion coefficient
δ_{ij}	delta function
ε_0	permittivity of free surface or region designated by Ω_2
ε	emissivity
ε_p	penalty parameter
$\partial\Omega$	boundary of computational domain
∇	gradient operator
ϕ	shape function
Φ	electric potential
γ	surface tension
κ	geometric parameter for elliptical functions
η	molecular viscosity
ρ	density
θ	θ-direction
σ_e	surface charge distribution
σ_s	Stefan–Boltzmann constant
Ω	computational domain
τ	stress tensor

Subscripts

d	droplet
i	the ith point
l	laser beam
1	region inside the droplet
2	region outside the droplet

Superscripts

i	the ith component
T	matrix transpose

cal properties of high melting point and corrosive melts can be measured without interference from the container walls. Moreover, it seems to be the only technique for measuring the physical properties of the undercooled melts [2].

Electrostatic levitation, developed based on the principle of electrostatics, is one of the containerless processing systems designed for these microgravity applications. The specific design of the system and its testing have been detailed elsewhere [1] and the basic idea is sketched in Fig. 1(a). A droplet is positively charged and immersed in an electric field generated by a group of electrodes that are at different potentials. This electric field interacts with the positive charges on the droplet to give rise to an electrostatic force, which is in the same direction as the electric field. If an appropriate combination of the electric field and charges is chosen, the electrostatic force (or the Coulomb force) can be strong enough to support the weight of the droplet in normal gravity. In practical design, an additional feedback control system is also used to accurately position the droplet and stabilize the levitation process [1]. External heating must be supplied to heat or melt the levitated samples. This is

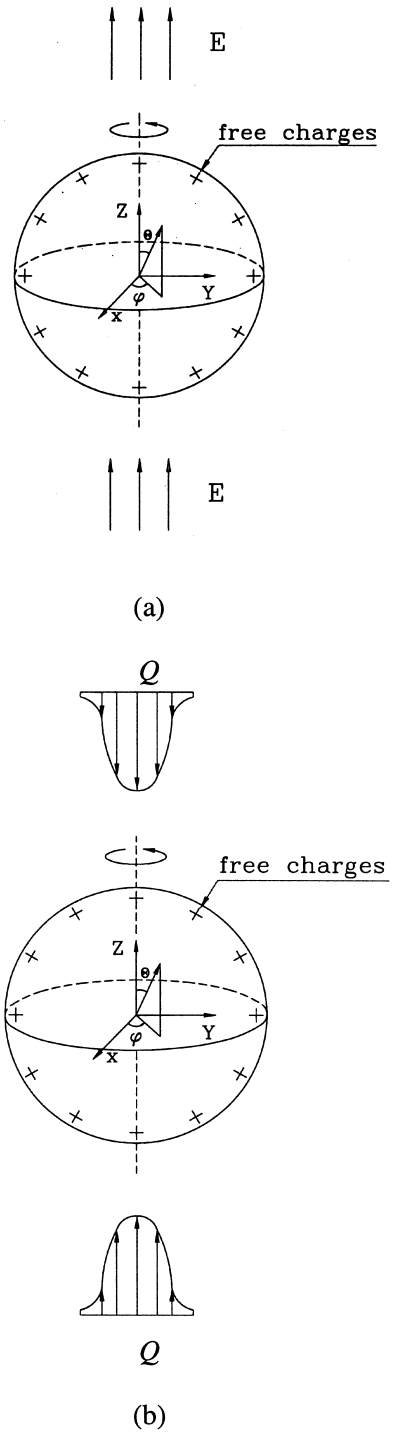

Fig. 1. Schematic representation of a positively charged melt droplet levitated in an electrostatic field: (a) leviation mechanism; (b) laser heating arrangement.

achieved by either UV-rich high-pressure xenon arc lamps or laser beams. The entire operation is carried out in a high vacuum chamber to prevent gas breakdown. At present, a sample of approximately 200 mg can be levitated electrostatically under earthbound conditions and extensive testing is being made to study the feasibility of its application in microgravity [3].

Electrostatic levitation has some attractive advantages over levitation by other techniques, such as magnetic fields. Perhaps, one of the most important advantages of electrostatic levitation is that, in principle, it can support a wider range of materials including metals, semiconductors and insulators, while magnetic levitation is limited to electrical conductors only. Also, for electrically conducting samples levitated in vacuum, there will be no internal flows that are attributed to the application of the electric field, because the droplet maintains an equal potential over the entire melt and thus the Maxwell stress inside the sample is uniform [4–6]. This may be extremely important for some planned experiments involving the measurement of certain thermophysical properties, such as melt viscosity and surface tension by induced droplet oscillation in microgravity. In contrast, vigorous recirculating flow occurs in melt droplets supported by magnetic levitation, particularly that induced by surrounding coils intended for heating or squeezing [7–12].

So far, very little information is available on the fundamental behavior of droplets levitated in electric fields [1–3,13,14]. The existing work on electrostatic levitation is primarily concerned with system design and the feedback control mechanism [1–3]. There also have been some analyses of an inviscid oscillation of charged drops for simple electric field configuration and shape stability [13,14]. Information about transport phenomena in electrostatically levitated droplets is very scarce, however. Experience with earthbound electrostatic levitation has suggested that internal fluid flow may occur in levitated drops [2,3]. While electrostatic forces are not responsible for an internal flow in a conducting sample, internal flows can arise from other sources. For example, under terrestrial conditions, natural convection occurs due to a temperature difference in the droplet. Since the droplet size is small, surface tension driven flow or Marangoni convection may become important for the levitated droplets in both normal and micro gravity. Also, an electric field induces a non-uniform distribution of electric pressure along the surface of a droplet. As such, a droplet cannot maintain a spherical shape in an electrical field, and its final shape is determined as a result of a local force balance along the free surface. Undoubtedly, an understanding of these physical phenomena is of critical value for both the design of electrostatic levitation systems and the planning of related experiments.

In this paper we study two critical issues concerning the fundamental behavior of a droplet levitated in an electrostatic field, that is, the electrostatically induced free surface deformations and thermally induced internal fluid flows. Towards this end, a computational methodology is developed for the prediction of the electrostatic deformation of, and internal fluid flows in the droplets under terrestrial and microgravity conditions. The motivation for normal gravity studies comes from the fact that the actual device is developed on earth and extensive ground-based experiments are conducted before it is finally installed in the International Space Station. In developing the computational algorithms, the boundary element method is used for the solution of the electrostatic field distribution, and is coupled with the weighted residuals method for an iterative solution of the equilibrium free surface shapes of the levitated droplet. The temperature distribution and fluid flow field in the droplets are calculated using the finite element method. Numerical simulations are carried out for various conducting materials for electrostatic levitation experiments under both earthbound and microgravity conditions.

2. Mathematical formulation

The problem under consideration is illustrated in Fig. 1. A liquid sphere, charged positively, is suspended in an electrostatic field generated by two horizontal, parallel electrodes placed far apart (Fig. 1(a)). The droplet is heated by two laser beams in the areas around the north and south poles (Fig. 1(b)). The statement of the problem of drop shapes and internal flows should include the formulations for the electric field and the thermal and fluid flow fields. The electric field is described by the Maxwell equations, which for the present problem simplify to a partial differential equation involving only the electric potential. For an electrically conducting droplet such as a molten silicon or metal droplet, only the electric potential outside the droplet is needed because the electric field inside the droplet is identically zero by the Gauss law [15]. Thus, the equations governing the electric potential distribution in the region outside the droplet may be written as follows,

$$\nabla^2 \Phi = 0 \quad \in \Omega_2 \tag{1}$$

$$\Phi = \Phi_0 \quad \in \Omega_1 \cap \Omega_2 \tag{2}$$

$$\varepsilon_0 \mathbf{n} \cdot \nabla \Phi = -\sigma_e \quad \in \Omega_1 \cap \Omega_2 \tag{3}$$

$$\oiint_{\partial \Omega_1} \sigma_e \, ds = -\oiint_{\partial \Omega_1} \varepsilon_0 \mathbf{n} \cdot \nabla \Phi \, ds = Q \quad \in \Omega_1 \cap \Omega_2 \tag{4}$$

$$\Phi = -E_0 R \cos\theta \quad R \to \infty \tag{5}$$

with Φ_0 being the unknown constant potential of the surface of the droplet, which is calculated by the surface integral representing charge conservation, as expressed in Eq. (4). The last equation states the fact that the applied electric field is uniform and points to the positive z-direction.

The mathematical description of the fluid flow and temperature distribution in the electrostatically levitated melt droplet is given by the Navier–Stokes equation and the thermal energy balance equation [16], viz.,

$$\nabla \cdot \mathbf{u} = 0 \quad \in \Omega_1 \tag{6}$$

$$\begin{aligned} &\rho \frac{\partial \mathbf{u}}{\partial t} + \rho \mathbf{u} \cdot \nabla \mathbf{u} \\ &\quad = -\nabla p + \nabla \cdot \eta \left(\nabla \mathbf{u} + \nabla \mathbf{u}^{\mathrm{T}} \right) - \rho \beta \mathbf{g} (T - T_r) \\ &\quad \in \Omega_1 \end{aligned} \tag{7}$$

$$\rho C_p \frac{\partial T}{\partial t} + \rho C_p \mathbf{u} \cdot \nabla T = \nabla \cdot k \nabla T \quad \in \Omega_1 \tag{8}$$

To solve the above fluid flow and heat transfer equations, mechanical and thermal boundary conditions are needed. These boundary conditions describe the physical constraints for the problem and are given below,

$$\begin{aligned} &-k \mathbf{n} \cdot \nabla T = \varepsilon \sigma_s \left(T^4 - T_\infty^4 \right) - Q_o \mathrm{e}^{-r_1^2 / a_1^2} \\ &\quad \in \Omega_1 \cap \Omega_2 \end{aligned} \tag{9}$$

$$\mathbf{u} \cdot \mathbf{n} = 0 \quad \in \Omega_1 \cap \Omega_2 \tag{10}$$

$$\mathbf{t} \cdot \tau \cdot \mathbf{n} = \frac{\mathrm{d}\gamma}{\mathrm{d}T} \mathbf{t} \cdot \nabla T \quad \in \Omega_1 \cap \Omega_2 \tag{11}$$

$$\mathbf{n} \cdot \bar{\sigma} \cdot \mathbf{n} = 2\gamma H \quad \in \Omega_1 \cap \Omega_2 \tag{12}$$

The last equation represents the flow induced by surface tension force that is a function of temperature along the surface of the droplet. The last equation represents the normal stress balance along the surface of the droplet.

3. Numerical solutions

3.1. Computation of electric field

Information on electric field distribution is required

to solve for the Maxwell stress distribution along the droplet surface, which contributes to the free surface deformation. Since the potential inside the droplet is constant, only the potential distribution outside needs to be solved for. Among all the numerical techniques available, the boundary element method is the most attractive choice for the solution. This is because the boundary condition at infinity can be directly incorporated into the boundary integral formulation, thereby reducing both computational time and storage requirement.

Since the detailed numerical procedure by which the boundary integral formulation is developed for the problem has been described elsewhere [17–19], only an outline is given here. To apply the boundary integral method and incorporate the boundary condition at $R\to\infty$, an intermediate variable $\Phi' = \Phi + E_o R\cos\theta$ is used and hence the boundary condition for Φ' becomes $\Phi' = 0$ at $R\to\infty$. With this, the standard procedure for employing the Green's function leads to the following boundary integral for Φ',

$$C(\mathbf{r}_i)\Phi'(\mathbf{r}_i) + \oint_{\partial\Omega_2} \Phi'(\mathbf{n}\bullet\nabla G)r\,\mathrm{d}\Gamma + \oint_{\partial\bar{\Omega}_2} \Phi'(\mathbf{n}\bullet\nabla G)r\,\mathrm{d}\Gamma = \oint_{\partial\Omega_2} G(\mathbf{n}\bullet\nabla\Phi')r\,\mathrm{d}\Gamma + \oint_{\partial\bar{\Omega}_2} G(\mathbf{n}\bullet\nabla\Phi')r\,\mathrm{d}\Gamma \tag{13}$$

where $\partial\Omega_2$ designates the surface of the droplet and $\partial\bar{\Omega}_2$ the boundary at infinity. The Green's function and its normal derivative are calculated by the following expressions written for a cylindrical coordinate system,

$$G(\mathbf{r}_i,\mathbf{r}) = \frac{4}{\sqrt{(r_i+r)^2+(z-z_i)^2}}K(\kappa) \tag{14}$$

$$\frac{\partial G}{\partial n} = \frac{4}{\sqrt{(r+r_i)^2+(z-z_i)^2}}\left\{\frac{n_r}{2r}\left[E(\kappa)-K(\kappa)\right] - \frac{n_r(r-r_i)+n_z(z-z_i)}{(r-r_i)^2+(z-z_i)^2}E(\kappa)\right\} \tag{15}$$

where κ is the geometric parameter calculated by

$$\kappa^2 = \frac{4r_i r}{(r_i+r)^2+(z_i-z)^2} \tag{16}$$

The two integrals involving $\partial\bar{\Omega}_2$ represent the contribution from the boundary at $R\to\infty$ with the following asymptotic behavior of G and Φ',

$$\Phi'(r_i,R)\approx O(R^{-2}),\ \frac{\partial\Phi'}{\partial n}(r_i,R)\approx O(R^{-3}) \quad \text{as } R\to\infty \tag{17}$$

$$G(r_i,R)\approx O(R^{-2}),\ \frac{\partial G}{\partial n}(r_i,R)\approx O(R^{-3}) \quad \text{as } R\to\infty \tag{18}$$

and also $\mathrm{d}\Gamma = R(\theta)\,\mathrm{d}\theta$, the two integrals each approach zero as $R\to\infty$ [19],

$$\oint_{\partial\bar{\Omega}_2} \Phi(\mathbf{n}\cdot\nabla G)r\,\mathrm{d}\Gamma\to 0 \quad \text{and} \quad \oint_{\partial\bar{\Omega}_2} G(\mathbf{n}\cdot\nabla\Phi)r\,\mathrm{d}\Gamma\to 0 \quad \text{as } R\to\infty \tag{19}$$

Thus, Eq. (13) simplifies to a boundary integral that involves only the surface of the droplet, $\partial\Omega_2$. The boundaries of Ω_2 can be discretized into small segments and the boundary integrals may be rewritten as a sum of the integral contributions from individual boundary elements. Further, with $\Phi = \Phi' - E_0 r\cos\theta$ substituted into the resultant equation, one has the following boundary integral formulation,

$$C_i\Phi(\mathbf{r}_i) + \sum_{j=1}^{N}\int_{\partial\Omega_{2,j}} \Phi\frac{\partial G}{\partial n}\,\mathrm{d}\Gamma = \sum_{j=1}^{N}\int_{\partial\Omega_{2,j}} \frac{\partial\Phi}{\partial n}G\,\mathrm{d}\Gamma + \sum_{j=1}^{N}\int_{\partial\Omega_{2,j}} E_0 n_z G\,\mathrm{d}\Gamma - \sum_{j=1}^{N}\int_{\partial\Omega_{2,j}} E_0 z\frac{\partial G}{\partial n}\,\mathrm{d}\Gamma - C_i E_0 z_i \tag{20}$$

where N is the total number of boundary elements lying along the entire boundary of Ω_2. Following the standard boundary element discretization and noticing that the potential on the surface is a constant, one obtains the final matrix form for the unknowns on the surface of the droplet,

$$\mathbf{H}\{\Phi_0\} = -\mathbf{G}\left\{\frac{\partial\Phi}{\partial n}\right\} + E_0\mathbf{G}\left\{\frac{\partial z}{\partial n}\right\} - \mathbf{H}E_0\{z\} \tag{21}$$

where $\mathbf{H}$ and $\mathbf{G}$ are the coefficient matrices involving the integration of $\partial G/\partial n$ and G over a boundary element. To complete the solution, Eq. (4) is discretized and solved along with the above equation to obtain the surface distribution of $\partial\Phi/\partial n$ and the constant Φ_0.

3.2. Computation of free surface shapes

For the purpose of droplet shape calculations, the normal stress balance equation (Eq. (12)) along the

droplet surface can be more conveniently written in a spherical coordinate system,

$$\frac{\gamma}{R^2\sin\theta}\left[\frac{(2R^2+R_\theta^2)\sin\theta}{\sqrt{R^2+R_\theta^2}}-\frac{\mathrm{d}}{\mathrm{d}\theta}\left(\frac{RR_\theta\sin\theta}{\sqrt{R^2+R_\theta^2}}\right)\right]$$

$$=-P_\mathrm{o}-\rho gR\cos\theta+\frac{\varepsilon_0(\mathbf{n}\cdot\nabla\Phi)^2}{2} \tag{22}$$

In writing the above equation, we have also neglected dynamic pressure and viscous contribution to facilitate the computations [19]. This simplifies the drop deformation calculation by decoupling it from the fluid flow calculation. As discussed in Section 3.4, this simplification is valid for the cases reported in this study. The above equation may be solved using the Weighted Residuals Method once the normal derivative of the potential field is known along the droplet surface. To derive the weighted residuals formulation, the surface of the droplet is discretized and defined by R_i, the distance between the surface node and the center of the droplet. By multiplying the above equation by a weighting function ψ_i, followed by integration by parts, one has the final equation for the surface coordinates R,

$$\int_0^\pi\left\{\gamma\frac{RR_\theta\frac{\mathrm{d}\psi_i}{\mathrm{d}\theta}+\psi_i(2R^2+R_\theta^2)}{\sqrt{R^2+R_\theta^2}}+R^2\psi_i\left(P_0+\rho gR\cos\theta-\frac{\varepsilon_0(\mathbf{n}\cdot\nabla\Phi)^2}{2}\right)\right\}\sin\theta\,\mathrm{d}\theta$$

$$=0 \tag{23}$$

where the variables R and R_θ are calculated by

$$R=\sum_{i=1}^{Ne}\psi_iR_i\quad\text{and}\quad R_\theta=\sum_{i=1}^{Ne}R_i\frac{\mathrm{d}\psi_i}{\mathrm{d}\xi}\frac{\mathrm{d}\xi}{\mathrm{d}\theta}$$

The constraints of the volume conservation and the center of the mass of the electrostatically levitated droplet are needed to determine the droplet shape and position. The two constraints are expressed as

$$\frac{1}{a_\mathrm{d}^3}\int_0^\pi R^3\sin\theta\,\mathrm{d}\theta=2 \tag{24}$$

$$\frac{3}{8a_\mathrm{d}^3}\int_0^\pi R^4\cos\theta\sin\theta\,\mathrm{d}\theta=z_\mathrm{c} \tag{25}$$

where z_c is the center of mass. The free surface may be discretized into N elements and Eqs. (23)–(25) are integrated numerically. The final results are expressed as a set of algebraic equations, which are then solved for the unknowns R_i, K and z_c [17,19].

3.3. Computation of thermal and fluid flow fields

The governing equations for the thermal and fluid flow fields along with the boundary conditions are solved using the Galerkin finite element method. Since details are well documented in many textbooks, only an outline is given here. In essence, the computational domain is first divided into small elements. Within each element, the dependent variables $\mathbf{u}$, P and T are interpolated by shape functions of ϕ, ψ, and θ,

$$\boldsymbol{u}^i(x,t)=\phi^\mathrm{T}\mathbf{U}^i(t) \tag{26}$$

$$P(x,t)=\psi^\mathrm{T}\mathbf{P}(t) \tag{27}$$

$$T(x,t)-T_\mathrm{r}=\theta^\mathrm{T}\mathbf{T}(t) \tag{28}$$

where $\mathbf{U}^i$, $\mathbf{P}$ and $\mathbf{T}$ are column vectors of element nodal point unknowns.

Substituting the above equations into the governing equations, we get the residuals R_1, R_2 and R_3 which represent the momentum, mass conversion and energy equations respectively. The Galerkin form of the Method of Weighted Residuals seeks to reduce these errors to zero, and the shape functions are chosen the same as the weighting functions. Following the procedures given in [17], the governing equations for the fluid flow and heat transfer may be re-written as

$$\left(\int_{\Omega_1}\psi(\hat{i}\cdot\nabla\phi^\mathrm{T}+\delta_{2i}\phi^\mathrm{T}/r)\,\mathrm{d}V\right)\mathbf{U}^i=-\varepsilon\left(\int_{\Omega_1}\psi\psi^\mathrm{T}\,\mathrm{d}V\right)\mathbf{P} \tag{29}$$

$$\left(\int_{\Omega_1}\rho\phi\phi^\mathrm{T}\,\mathrm{d}V\right)\frac{\mathrm{d}\mathbf{U}^i}{\mathrm{d}t}+\left(\int_{\Omega_1}\rho\phi\mathbf{u}\cdot\nabla\phi^\mathrm{T}\,\mathrm{d}V\right)\mathbf{U}^i-\left(\int_{\Omega_1}(\hat{i}\cdot\nabla\phi+\delta_{2i}\phi/r)\psi^\mathrm{T}\,\mathrm{d}V\right)\mathbf{P}+\left(\int_{\Omega_1}\eta(\nabla\phi\cdot\nabla\phi^\mathrm{T}+2\delta_{2i}\phi\cdot\phi^\mathrm{T}/r^2)\,\mathrm{d}V\right)\mathbf{U}^i+\left(\int_{\Omega_1}\eta(\hat{i}\cdot\nabla\phi)(\hat{j}\cdot\nabla\phi^\mathrm{T})\,\mathrm{d}V\right)\mathbf{U}^j+\left(\int_{\Omega_1}\rho\beta\phi\theta^\mathrm{T}\hat{i}\cdot\boldsymbol{g}\right)\mathbf{T}=\int_{\partial\Omega_1}\mathbf{n}\cdot\bar{\sigma}\cdot\hat{i}\phi\,\mathrm{d}s \tag{30}$$

$$\left(\int_{\Omega_1}\rho C_p\theta\theta^{\mathrm{T}}\,\mathrm{d}V\right)\frac{\mathrm{d}\mathbf{T}}{\mathrm{d}t}+\left(\int_{\Omega_1}\rho C_p\theta\mathbf{u}\cdot\nabla\theta^{\mathrm{T}}\,\mathrm{d}V\right)\mathbf{T}+\left(\int_{\Omega_1}k\nabla\theta\cdot\nabla\theta^{\mathrm{T}}\,\mathrm{d}V\right)\mathbf{T}=-\int_{\partial\Omega_1}q_T\theta\,\mathrm{d}s \tag{31}$$

Once the form of shape functions ϕ, θ, and ψ is specified, the integrals defined in the above equations can be expressed by the matrix equation. The momentum and energy equations may be combined into a single global matrix equation,

$$\begin{bmatrix}\mathbf{M} & 0\\ 0 & \mathbf{N}_T\end{bmatrix}\begin{bmatrix}\dot{\mathbf{U}}\\ \dot{\mathbf{T}}\end{bmatrix}+\begin{bmatrix}\mathbf{A}(\mathbf{U})+\mathbf{K}+\frac{1}{\varepsilon_{\mathrm{p}}}\mathbf{E}\mathbf{M}_{\mathrm{p}}^{-1}\mathbf{E}^{\mathrm{T}} & \mathbf{B}\\ 0 & \mathbf{D}_T(\mathbf{U})+\mathbf{L}_T\end{bmatrix}\times\begin{bmatrix}\mathbf{U}\\ \mathbf{T}\end{bmatrix}=\begin{bmatrix}\mathbf{F}\\ \mathbf{G}_T\end{bmatrix} \tag{32}$$

Note that in constructing the above element matrix equation, the penalty formulation has been applied, and $\mathbf{P}$ in the momentum equation is substituted by $\frac{1}{\varepsilon_{\mathrm{p}}}\mathbf{M}_{\mathrm{p}}^{-1}\mathbf{E}^{\mathrm{T}}\mathbf{U}$. The coefficient matrices in the above equation are defined by:

$$\mathbf{M}_{\mathrm{p}}=\int_{\Omega_1}\psi\psi^{\mathrm{T}}\,\mathrm{d}V$$

$$\mathbf{M}=\int_{\Omega_1}\theta\theta^{\mathrm{T}}\,\mathrm{d}V$$

$$\mathbf{L}_T=\int_{\Omega_1}k\nabla\theta\cdot\nabla\theta^{\mathrm{T}}\,\mathrm{d}V$$

$$\mathbf{D}_T(\mathbf{U})=\int_{\Omega_1}\rho C_p\theta\mathbf{u}\cdot\nabla\theta^{\mathrm{T}}\,\mathrm{d}V$$

$$\mathbf{G}_T=-\int_{\partial\Omega_1}q_T\theta\,\mathrm{d}s$$

$$\mathbf{K}_{ij}=\left(\int_{\Omega_1}\eta(\nabla\phi\cdot\nabla\phi^{\mathrm{T}}+2\delta_{2i}\phi\cdot\phi^{\mathrm{T}}/r^2)\,\mathrm{d}V\right)\delta_{ij}+\int_{\Omega_1}\eta(\hat{i}\cdot\nabla\phi)(\hat{j}\cdot\nabla\phi^{\mathrm{T}})\,\mathrm{d}V$$

$$\mathbf{N}_T=\int_{\Omega_1}\rho C_{\mathrm{p}}\theta\theta^{\mathrm{T}}\,\mathrm{d}V$$

$$\mathbf{E}_i=\int_{\Omega_1}(\hat{i}\cdot\nabla\phi+\delta_{2i}\phi/r)\psi^{\mathrm{T}}\,\mathrm{d}V$$

$$\mathbf{A}(\mathbf{U})=\int_{\Omega_1}\rho\phi\mathbf{u}\cdot\nabla\theta^{\mathrm{T}}\,\mathrm{d}V$$

$$\mathbf{B}=\int_{\Omega_1}\rho\beta\mathbf{g}\phi\theta^{\mathrm{T}}\,\mathrm{d}V$$

$$\mathbf{F}=\int_{\partial\Omega_1}\phi\tau\cdot\mathbf{n}\,\mathrm{d}s$$

where $\mathbf{U}$ is a global vector containing all nodal values of u and v. The assembled global matrix equations are stored in the skyline form and solved using the Gaussian elimination method. The successive substitution method is applied for nonlinear iteration and the time derivatives are approximated using the implicit finite difference scheme.

3.4. Numerical procedures

Computer codes are developed for the above finite element and boundary element formulations. Numerical details are given in other publications [17,18,21]. A variety of element types is available in the programs. The elliptical integrals in the boundary integral formulation are calculated using the formulae given in [19] and the boundary element terms involving singularity are calculated analytically, following a similar procedure as described by Li and Evans [20].

The algorithm entails the calculation of surface profiles and both transient and state steady thermal and fluid flow fields. The computation of the free surface shapes of a droplet levitated in an electrostatic field requires an iterative procedure. To simplify the calculations dynamic pressure is neglected, and thus only the balance between the surface tension and electrostatic pressure is considered (see Eq. (24)). To determine dynamic pressure and the viscous flow effect and to check the validity of Eq. (24), calculations of free surface deformation with fluid flow included were also made for a selection number of cases. Results show that the dynamic pressure and viscous stresses together contribute less than 2% for the cases studied, but their inclusion increases the computational time substantially, since the fluid flow field has to be now included in the iteration loop. Thus, for the cases presented below, Eq. (24) was used and the dynamic pressure and viscous stresses were neglected. The iteration for shape calculations starts with a guessed free surface shape, then the calculation of the electric field and hence the electrostatic pressure along the surface. Eqs. (23)–(25) are solved with the input of the electrostatic

Table 1
Parameters used in calculations

Metal	Cu	Fe	Ni	Zr	Ga	Si
T_{melt} (K)	1357.8	1809	1728	2125	302.7	1685
Q_0 (W/m^2)	0.7×10^6	2.5×10^6	2.0×10^6	4.5×10^6	10^3	1.5×10^6
a_d (mm)	1.8	1.8	1.8	1.8	1.8	2.5
a_l (mm)	0.9	0.9	0.9	0.9	0.9	1.25
ρ (kg/m^3)	8000	7015	7905	5800	6090	2510
μ (kg/m s)	4×10^{-3}	5.5×10^{-3}	4.9×10^{-3}	8.0×10^{-3}	2.04×10^{-3}	0.94×10^{-3}
γ (N/m)	1.285	1.872	1.778	1.480	0.718	0.864
$d\gamma/dT$ (N/m K)	-1.3×10^{-4}	-4.9×10^{-4}	-3.8×10^{-4}	-2.0×10^{-4}	-1.0×10^{-4}	-1.3×10^{-4}
K (W/m K)	176.3	78.2	88.5	22.6	39.2	138.5
C_p (J/kg K)	495	795	620	289	389	1040
E (V/m)	3×10^6	3×10^6	3×10^6	3×10^6	2×10^6	2.5×10^6
Q_c/ε_0 (Cm/F)	731.2	882.5	860.1	784.7	546.6	981.4
Emisivity ε	0.3	0.3	0.3	0.3	0.3	0.3
β (K^{-1})	20.3×10^{-6}	14.6×10^{-6}	16.3×10^{-6}	5.9×10^{-6}	18.3×10^{-6}	7.6×10^{-6}
Pr	1.123×10^{-2}	5.591×10^{-2}	3.433×10^{-2}	10.23×10^{-2}	2.024×10^{-2}	0.706×10^{-2}

pressure distribution, for the free surface shape. The calculated shape is fed back to determine an updated distribution of the electrostatic pressure, which in turn is used to obtain an updated free surface shape of the droplet. This iterative procedure continues until the unknowns converge within a preset tolerance [19]. With the shape so determined, the thermal and fluid flow fields are then computed using the finite element method described above.

4. Results and discussion

The computational algorithms developed above enable the prediction of the electric field distribution, the electric pressure distribution along the surface of a droplet, droplet shapes, temperature distribution and internal convection within the droplets driven by surface tension and buoyancy forces in normal gravity. A selection of computed results is presented for some typical materials being considered for microgravity applications. Unless otherwise indicated, the computations used the physical properties and parameters as given in Table 1[23]. It is noted that Q_c is the critical charge as predicted by Rayleigh's theory [22], above which a charged drop becomes unstable and starts to break into smaller droplets. The boundary element and finite element meshes used for the computation are illustrated in Fig. 2. A total of 48 linear boundary elements (as designated by heavy dots in Fig. 2) was used. The thermal and fluid flow calculations used 264 nine-node elements, with penalty formulation for pressure, and the density of the mesh was increased near the free surface to ensure accuracy. A convergence criterion of 1×10^{-4} was set for relative error associated with unknowns for free surface shapes, temperature and velocity. Different meshes and different mesh distributions were also used to check the mesh depen-

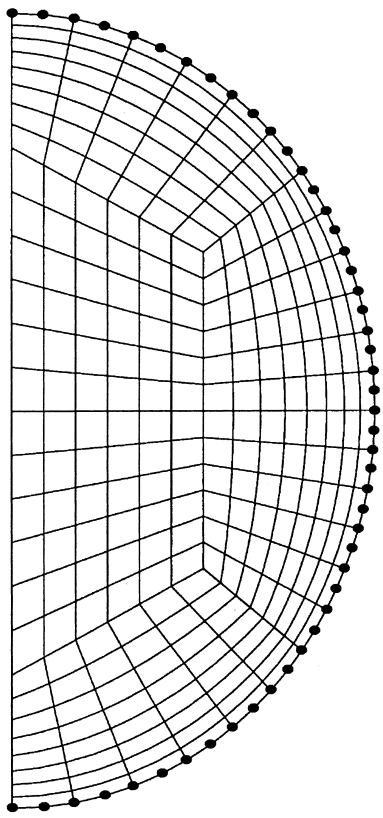

Fig. 2. Finite element mesh and boundary element discretization for numerical computations.

dency. The final mesh (see Fig. 2) used for the computations was determined such that any further refinement of the mesh produces an error smaller than 0.1% (relative to the final mesh).

Before they are applied to compute the results relevant to electrostatic levitation, the computer codes are checked against available solutions. For boundary element calculations, we consider an electrically conducting droplet of a perfect sphericity that is positively charged and immersed in a uniform electric field. For this idealized situation, an analytical solution may be obtained via the classical separation-of-variable method. The surface charge density distribution induced on the sphere by the applied electric field is a function of the applied electric field strength and varies along the surface. The analytical expression for this field quantity may be written as follows [15],

$$\sigma_e(\theta) = Q/4\pi a_d^2 + 3\varepsilon_0 E_0 \cos\theta \tag{33}$$

Fig. 3 compares the surface charge distribution obtained from the boundary formulation with the analytical solution given by Eq. (33) for the conducting sphere. Excellent agreement is obtained between the numerical and analytical solutions, thereby providing a validation of the boundary element formulation. The free surface deformation calculations and the fluid flow calculations were also checked with available analytical solutions for meniscus wetting near a vertical wall [24] and surface tension driven flows in a simple cavity [16]. The codes were also checked with numerical solutions obtained using other commercial codes. For all the tested cases, the comparison between our codes and others has the same or nearly the same accuracy as appears in Fig. 3 or matches within the machine's accuracy.

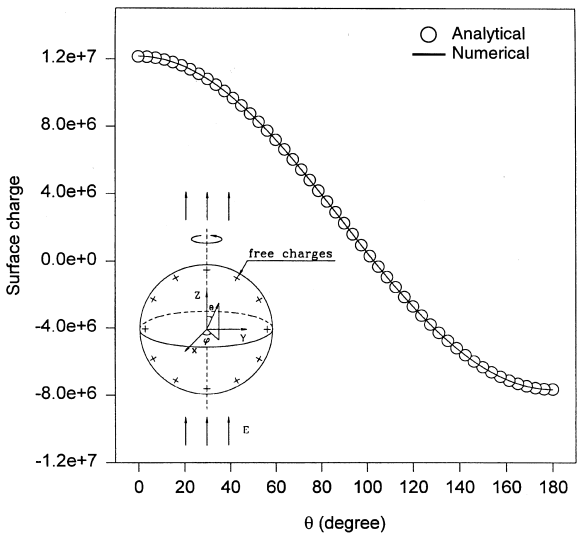

Fig. 3. Comparison of analytical and numerical solutions for the surface charge distribution in an electrically conducting sphere immersed in a uniform electric field.

4.1. Droplet shapes

For a droplet to be levitated in normal gravity, the total force acting on it must be zero, that is, the gravity force must be balanced by the total Coulomb force acting on the droplet, viz.,

$$m_d g = -\oiint_{\partial\Omega} P_e \mathbf{n}\cdot\hat{z}\,ds = E_0 Q \tag{34}$$

While a larger Q gives a bigger Coulomb force, there is an upper limit of Q for a droplet of given size and material (see Table 1), above which the shape of a droplet becomes unstable [22]. In selecting the electric field, its value should also be smaller than the breakout point for the gas environment. To circumvent this problem, a majority of the electrostatic levitation processes is carried out in a high vacuum environment.

While Eq. (34) represents the global balance that must be satisfied for a droplet to be levitated against gravity under terrestrial conditions, a local balance is required of forces involving gravity, electric pressure, and surface tension along the free surface of the droplet. The algorithm presented in Section 3.2 allows us to predict the profile of the free surface of a droplet when it is in mechanical equilibrium. Fig. 4 shows a

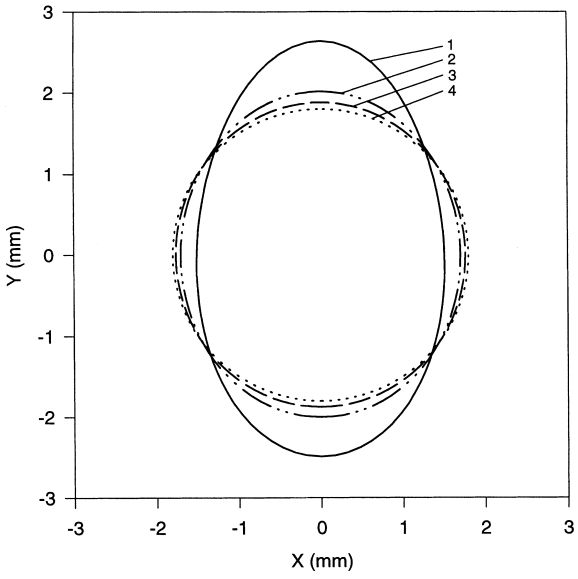

Fig. 4. Free surface profiles of a Cu droplet, electrostatically levitated in normal gravity: (1) $E_0 = 4\times10^6$ V/m and $Q = 0.3475\times10^{-9}$ C; (2) $E_0 = 3\times10^6$ V/m and $Q = 0.463\times10^{-9}$ C; (3) $E_0 = 2\times10^6$ V/m and $Q = 0.695\times10^{-9}$ C; (4) un-deformed liquid sphere.

set of the computed results for the free surface profiles of a copper droplet levitated in electric fields. In obtaining the results, Q and E_0 are chosen such that the above criterion for the global force balance (Eq. (34)) is met and that Q is smaller than Q_c. The shape of the initial un-deformed sphere is also plotted as a comparison. Examination of Fig. 4 illustrates that an electrostatically levitated droplet in normal gravity assumes a blob shape whose lower half surface is relatively flat. Numerical simulations with different applied conditions were also carried out. A different combination of Q and E_0, while maintaining the global balance, results in different equilibrium free surface profiles. For some cases, the droplet is deformed into a blob shape very similar to a rain drop during free fall [25]. When an increase in the electric field and a corresponding decrease in the applied charge occur simultaneously, the droplet becomes more elongated.

In microgravity, the electric forces are designed to position and confine a droplet because otherwise it would drift around in space, making it difficult to conduct meaningful measurements. The positioning is achieved by the concept of electrostatic levitation and a sophisticated feedback control mechanism [1]. Fig. 5 depicts a set of computed results for the free surface deformation of a droplet electrostatically positioned in microgravity. Since a net lifting force is not needed, the total net charge is equal to zero. However, as the droplet is placed in the electric field, the electric field is perturbed and induces surface charges on the droplet. These induced surface charges interact with the imposed electric field to ensure that the electric field inside the droplet is zero or the entire droplet is at a constant potential. Though the net force is zero, the local electric force along the surface is not, and must be balanced by the surface tension force, thereby defining a free surface profile for the droplet. Because the surface charges are negative on the lower half surface and positive on the upper half surface, they combine with an upward electric field to produce a force that pulls the surface away from the center. Moreover, the surface charges are symmetrically distributed because of the symmetry of the applied electric field. As a consequence, the droplet deforms symmetrically outward from the equator plane. A greater applied electric field results in a bigger surface charge, and hence a bigger pulling force. As such, a larger free surface deformation occurs with a droplet in a stronger electric field, as shown in Fig. 5.

To better assess the shape difference between normal gravity and microgravity, the electrostatically deformed free surface profiles are plotted in Fig. 6 for a Cu droplet, which has a diameter of 5 mm when undeformed. Clearly, in the case of normal gravity, the droplet assumes a blob shape. The lower part of the surface is flatter and the droplet points upward or in the direction opposite to the acceleration of gravity. This should not come as a surprise since the local elec-

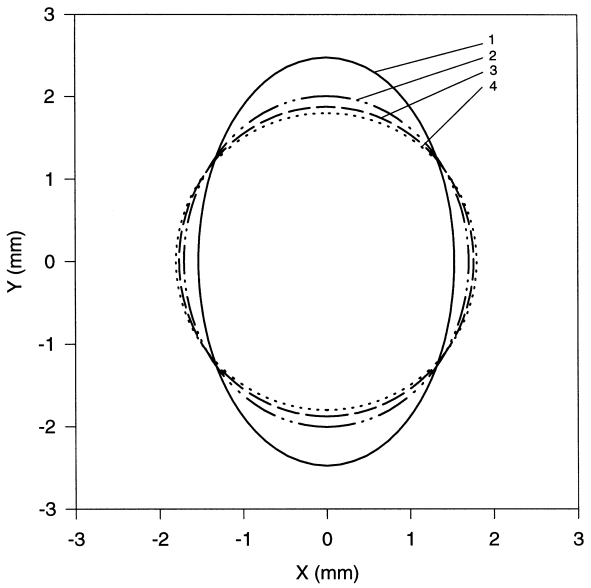

Fig. 5. Free surface deformation of a Cu droplet electrostatically positioned in microgravity ($Q = 0$): (1) $E_0 = 4 \times 10^6$ V/m; (2) $E_0 = 3 \times 10^6$ V/m; (3) $E_0 = 2 \times 10^6$ V/m; (4) un-deformed liquid sphere.

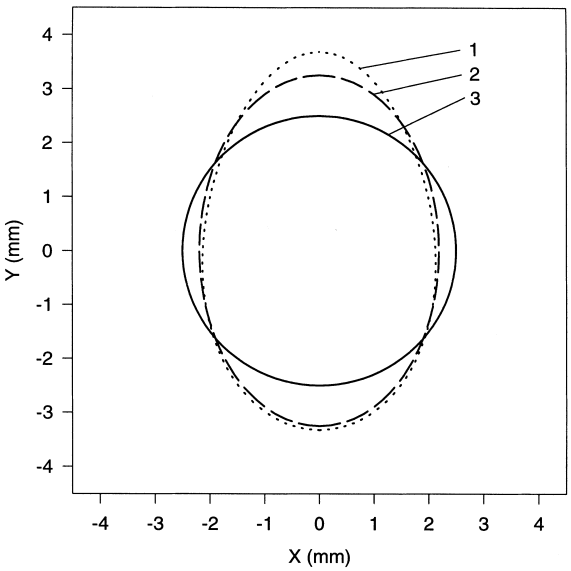

Fig. 6. Comparison of free surface profiles of a Cu droplet in normal and microgravity: (1) $E_0 = 3.3 \times 10^6$ V/m and $q = 1.56 \times 10^{-9}$ C (normal gravity); (2) $E_0 = 3.3 \times 10^6$ V/m and $Q = 0$ C (microgravity gravity); (3) un-deformed liquid sphere.

trostatic force points outward and tends to elongate the droplet in the two pole directions. With reference to Fig. 3, the surface charge attains a higher value on the upper surface than on the lower surface and thus a stronger pulling action results from the electric field, thereby giving rise to the final blob shape as shown in Fig. 6. In microgravity, the charge distribution is symmetric and thus the surface deformation is symmetric with respect to the equator plane.

4.2. Temperature distribution and internal convection

Let us now turn to the fluid flow and heat transfer aspects of an electrostatically levitated droplet. For an electrically conducting melt, the Maxwell stress is normal to the surface and there exist no tangential shear stress components. Because this stress field is non-vortical in nature, it generates no fluid motion in the droplet [4,5]. However, since the droplet is heated by laser beams at the two poles, a non-uniform temperature distribution arises in the droplet. For a droplet whose surface tension is a function of temperature such as those in Table 1, the non-uniform temperature distribution creates a non-uniform tangential stress on the surface of the droplet, which sets the fluid in motion [16].

Fig. 7 shows the temperature distribution and the fluid flow field inside a Cu droplet levitated in microgravity. The laser heating of the north and south pole regions gives rise to a symmetric temperature distribution in the droplet, as expected. A temperature difference of approximately 3 deg exists in the droplet, with the maximum temperatures at the poles. The temperature decreases from the poles to the equator

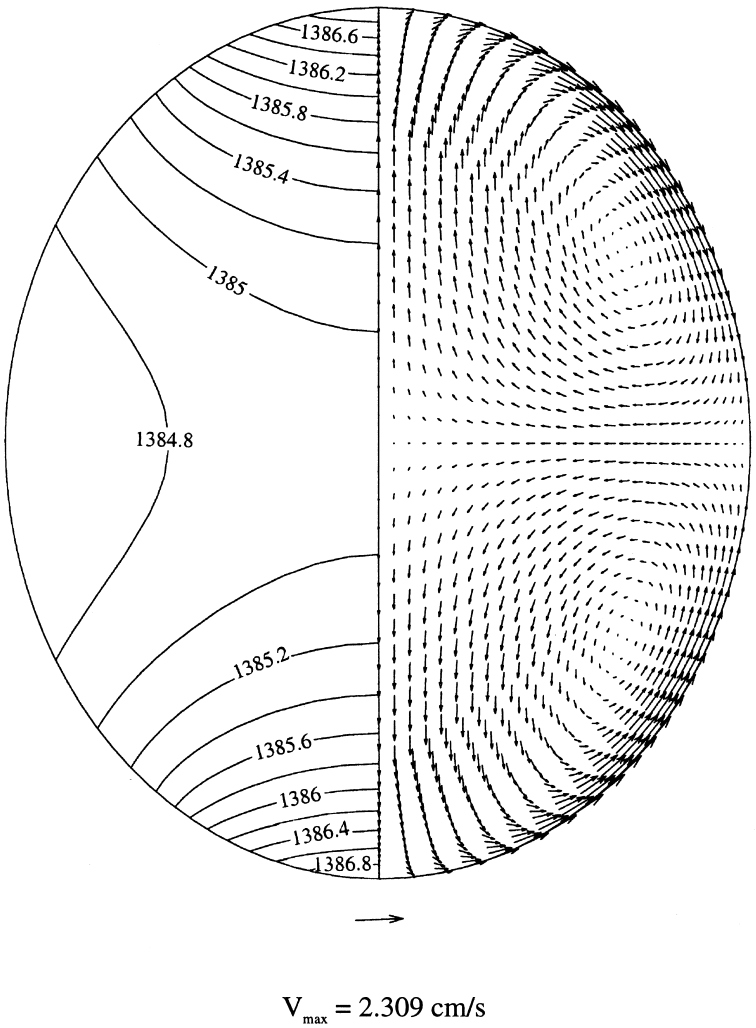

Fig. 7. Thermal contour and recirculating convection in a Cu droplet levitated in an electric field.

region, where the minimum temperature occurs. The temperature contour suggests that thermal transport in the droplet is primarily due to conduction and the internal convection hardly affects the thermal behavior. This is anticipated because the Prandtl number for Cu is small (see Table 1) and thermal diffusion predominates advection. The temperature difference causes a recirculating convection in the droplet such that the fluid particle moves from the high temperature region to the low temperature region on the surface, and inside the droplet moves from equator towards the pole regions. This fluid flow behavior may be explained below. Since the surface tension of Cu decreases with increasing temperature, a higher surface tension exists near the equator. The higher surface tension exerts a higher pulling force on the fluid element on the surface and thus drags the fluid towards that region from the lower surface tension (or higher temperature) part of the surface. To satisfy the flow continuity, the mass within the Cu droplet moves up from the equator to the pole regions, thereby forming an internal recirculating flow pattern.

Computed results show that a large temperature gradient and a higher flow velocity occur for a droplet with a high melting point for the same heating configuration. Fig. 8 illustrates the temperature distribution and fluid flow in a liquid Zr droplet in microgravity. The symmetric surface deformation is evident and is calculated using the free surface algorithm as described above. For this case, a temperature difference of 74 K exists in the droplet, and maximum velocity is as high as 25.41 cm/s. Experience with electrostatic levitation has indicated that a temperature difference of 50–80 K may exist in materials with a high melting point. This is supported by the calculations presented. In comparison with the results for the Cu droplet, the temperature contour clearly suggests that internal convection affects thermal transport in the droplet. Additional calculations showed that both maximum velocity and maximum/minimum temperature difference (ΔT) in the Zr droplet increase approximately linearly with the applied laser heating power (Q_0), as appears in Fig. 9. A similar linear relationship is found also for other materials in Table 1.

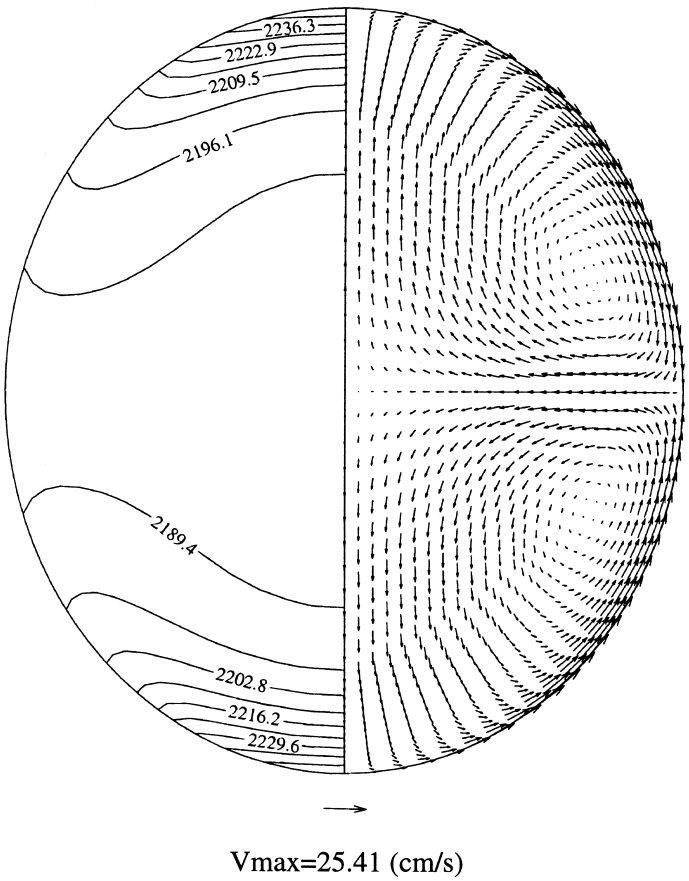

Fig. 8. Temperature distribution and recirculating Marangoni convection in a Zr droplet in an electrostatic field.

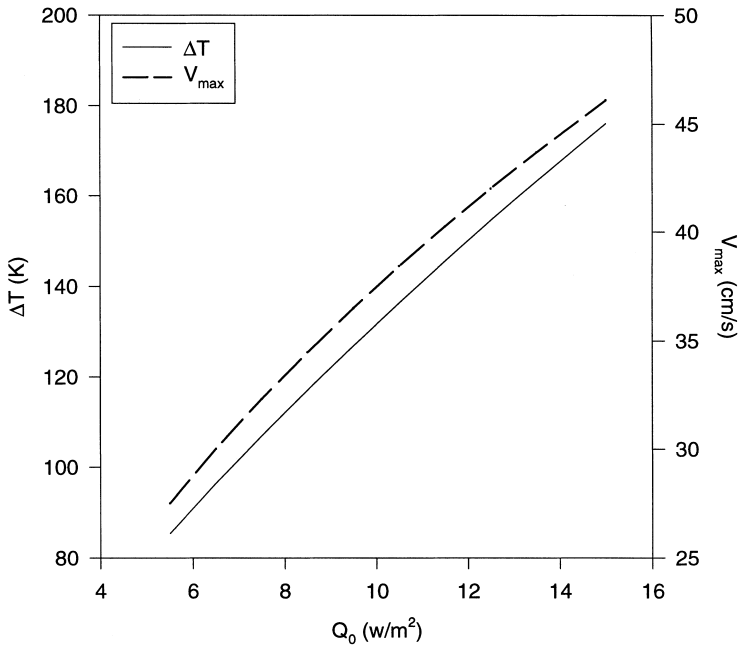

Fig. 9. Dependency of the maximum velocity and the maximum temperature difference on laser heating power.

The maximum velocity and temperature differences in droplets of other materials under consideration were also calculated and the results are summarized in Table 2. The computational procedures are the same as described above for the Cu and Zr droplets in that, first the free surface profiles are computed, followed by the calculations for the temperature and fluid flow fields. The thermal and velocity distributions are very similar to those described above.

Calculations of droplet surface deformations and thermal and fluid flow fields were also carried out for the materials under terrestrial conditions. The computed temperature contour and velocity profiles are very similar to those in microgravity and key results are given in Table 3. Comparison of Tables 2 and 3 indicates that for all cases considered here, buoyancy effects on the fluid flow are very small and internal flow in the electrostatically levitated droplets is primarily attributed to surface tension force gradients.

These results clearly suggest that to minimize internal convection, a more uniform temperature distribution is required, which in turn requires an appropriately distributed heating source. One of the simplest ways to better distribute the present heating source would be to increase the size of the laser beam. One such result is shown in Fig. 10, where the laser beam is assumed to cover the entire sphere (i.e. $a_l = a_d$). Clearly, the temperature difference is reduced by a factor of 7, which results in an almost four fold reduction in the maximum velocity. Compared with Fig. 8, the thermal contour is also different and shows a relatively smaller effect of convection on the temperature distribution.

Knowledge of the decay of both temperature and velocity fields in a levitated droplet, as it cools into an undercooling region, is crucial for the design of experiments for testing the fundamental solidification theory. In practice, when levitation is stabilized and the sample

Table 2
Results for micro-gravity condition

Metal	Cu	Fe	Ni	Zr	Ga	Si
ΔT (K)	2	15	13	74	0.02	10
$T_{min} - T_{max}$ (K)	1384–1386	1880–1895	1780–1793	2176–2250	337.51–337.53	1704–1714
V_{max} (cm/s)	2.309	17.16	13.01	25.41	0.0324	20.88
Re	83.1	394	377.8	322.5	1.74	1393.7
Ma	2.63	171.5	100.5	247	0.11	140.4

Table 3
Results for normal gravity condition

Metal	Cu	Fe	Ni	Zr	Ga	Si
ΔT (K)	3	15	13	74	0.01	10
$T_{min} - T_{max}$ (K)	1384–1387	1880–1895	1780–1793	2176–2250	337.60–337.61	1705–1715
T_{melt} (K)	1357.8	1809	1728	2125	302.7	1685
V_{max} (cm/s)	2.304	17.15	13.00	25.41	0.0326	21.04
σ/ε_0	72.2	63.29	71.32	52.33	78.5	72.8
Re	83.2	393.8	377.5	322.9	1.75	1404.6
Ra	0.158	1.14	1.08	1.34	0.0019	0.059
Ma	2.63	171.5	100.5	247	0.11	140.4

is heated to a designated temperature, the laser beam is turned off and the sample is allowed to cool below its melting point by losing heat to the environment. The computational methodology discussed above may be applied to predict the dynamic development of these transient thermal and fluid flow fields in electrostatically levitated droplets as they undergo undercooling.

Fig. 11 illustrates a set of snap shots of the time evolving velocity and temperature fields in a Zr droplet when the laser power is switched off and the droplet is allowed to cool approximately 200 K below the melting point. The calculations began with the initial velocity and temperature fields shown in Fig. 8. This set of results illustrates that the radiative loss of heat to

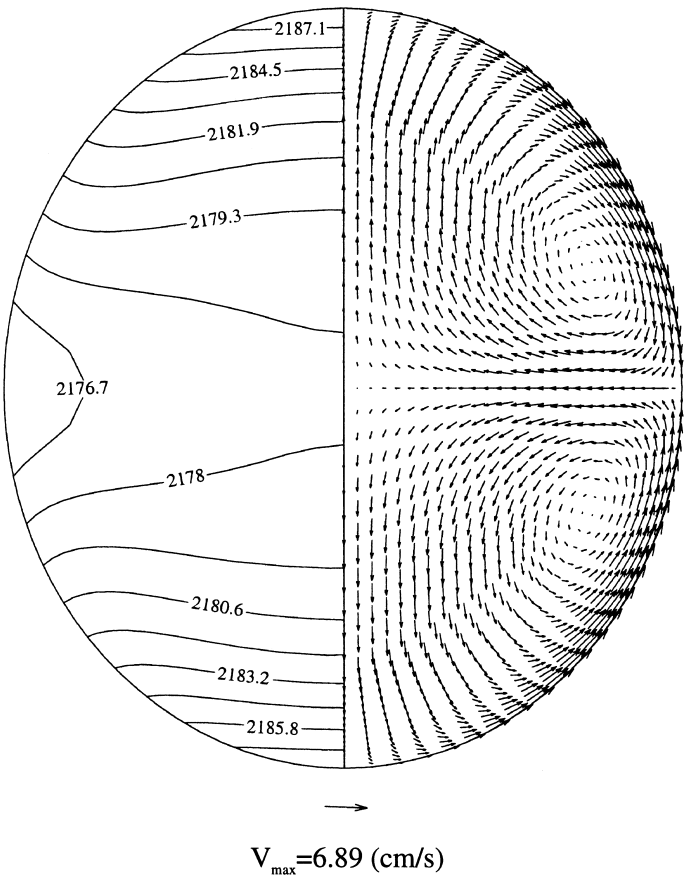

Fig. 10. Temperature distribution and internal velocity field in a Zr droplet with a larger laser heating beam diameter ($a_l = 1.8$ mm, $Q_0 = 0.67 \times 10^6$ w/m^2) in microgravity.

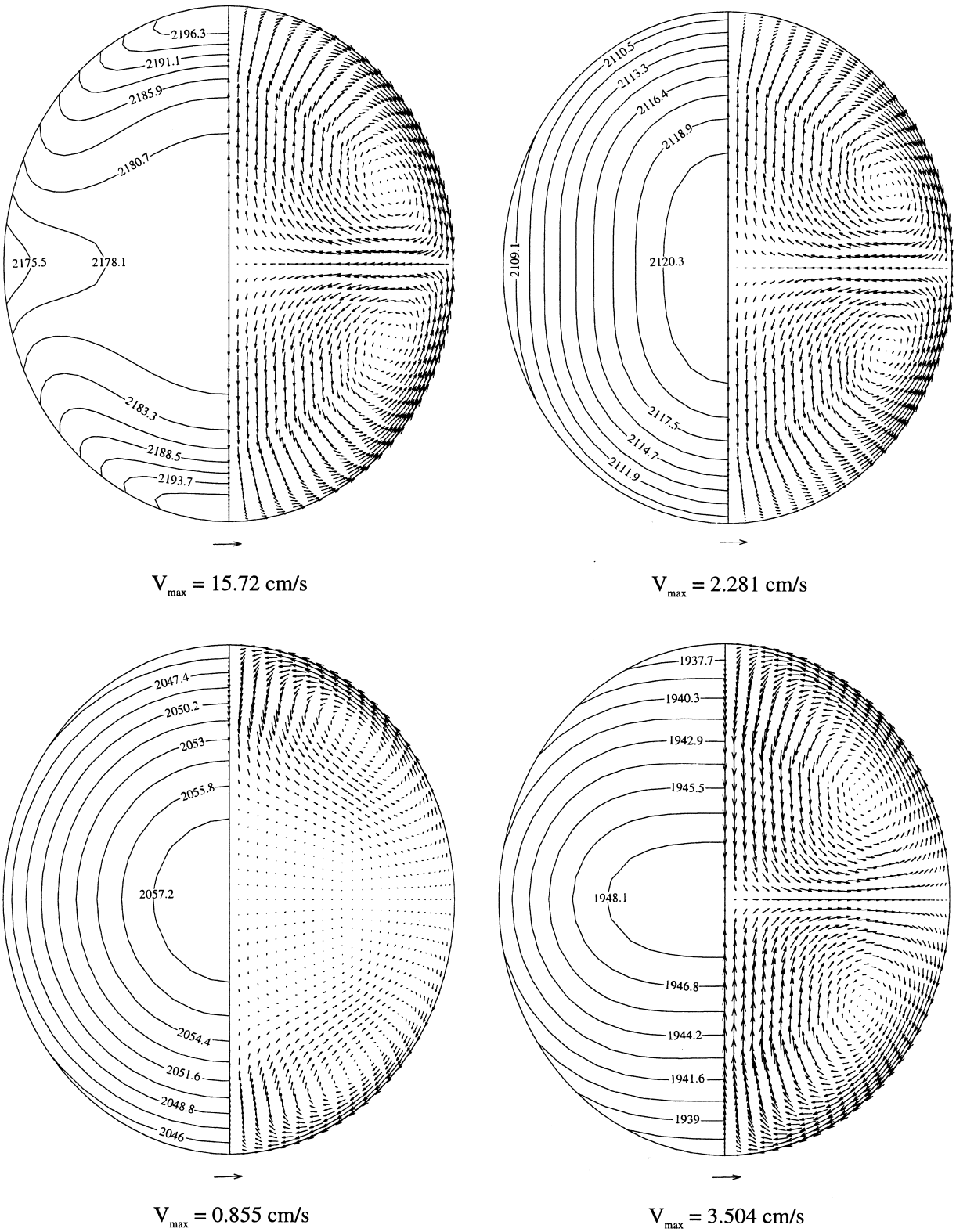

Fig. 11. Dynamic development of temperature and internal convection fields in a Zr droplet as it undergoes undercooling in microgravity: (a) $t = 0.01$ s; (b) $t = 0.2$ s; (c) $t = 0.4$ s; (d) $t = 0.8$ s.

the surroundings eventually results in temperature at the poles being lower and that at its center being higher. The temperature gradient along the surface also evolves such that the temperature at the equatorial gradually changes from being lower to higher than that at the two poles. This is more clearly illustrated in Fig. 12, where the temperature distribution along the droplet surface is plotted. This dynamic change in temperature leads to the evolution of the fluid flow field in the droplet. On the surface, the tangential velocity reverses its direction when the temperature at the equator plane becomes higher than that at the poles, as evidenced by the change of distribution of the tangential velocity with time, along the droplet surface that appears in Fig. 13. Examination of Fig. 11 shows that the flow near the surface reverses its direction of rotation at some point in time after cooling takes place. At this point two anti-rotating recirculating loops emerge in the droplet. The outer loop develops because the temperature at the poles is cooled below that at the equator plane, and hence the fluid particles are driven by the surface tension forces from the equator to the poles along the surface. The inner loop, on the other hand, is a carry-over from the initial flow field and is not sustainable. It becomes weaker and shrinks as the droplet gets cooler. Eventually, the inner loop loses its strength entirely and is engulfed by the outer loop.

Analytical solutions were obtained for the temperature decaying in levitated droplets [12,25]. The solutions were derived for magnetically levitated droplets by assuming that the droplets maintain sphericity and that the radiation boundary condition may be simplified to a Newton cooling boundary condition with an appropriate heat transfer coefficient. They may be adopted here for approximating the transient thermal and fluid flow fields in electrostatically levitated droplets by simply dropping out the terms associated with magnetic field effects, of course still subject to the geometric and thermal boundary condition restrictions. These analytical solutions are plotted in Fig. 14, along with the numerical results for the temperatures at some specific points. In calculating the thermal decay analytically, the heat transfer coefficient was evaluated using the average temperature between the initial and final temperatures. Numerical results plotted in Fig. 14 show that the temperature at the poles decays rapidly soon after cooling starts but the cooling rate decreases with time afterwards. The analytical solutions failed to predict the rapid change in temperature but gave nearly the same cooling rate as that computed numerically after the initial rapid decay. At the point where the laser beam was not present ($r = 1.72$ mm, $z = 0.$), the analytical and numerical results for the cooling curve match reasonably well for the entire cooling period. This and other similar comparisons suggest that the analytical solutions may be used to approximately estimate the thermal decay at the points that initially were not heated by laser beams.

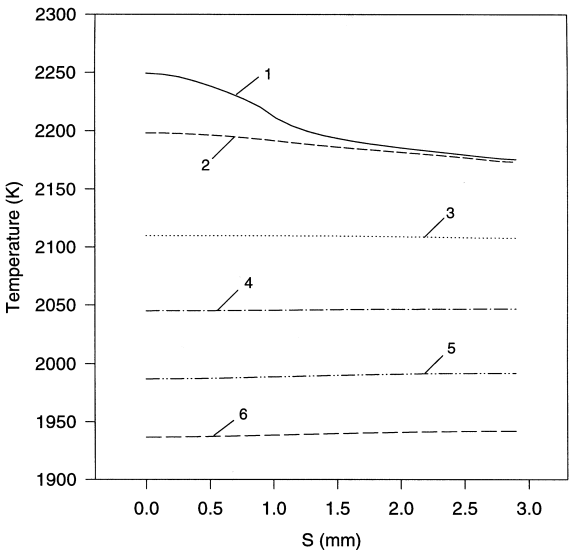

Fig. 12. Transient temperature distribution along the surface of the Zr droplet as it is cooled below its melting point in microgravity. S is measured from the north pole to the equator. Legends: (1) $t = 0$ s, (2) $t = 0.01$ s; (3) $t = 0.2$ s; (4) $t = 0.4$ s; (5) $t = 0.6$ s; (6) $t = 0.8$ s.

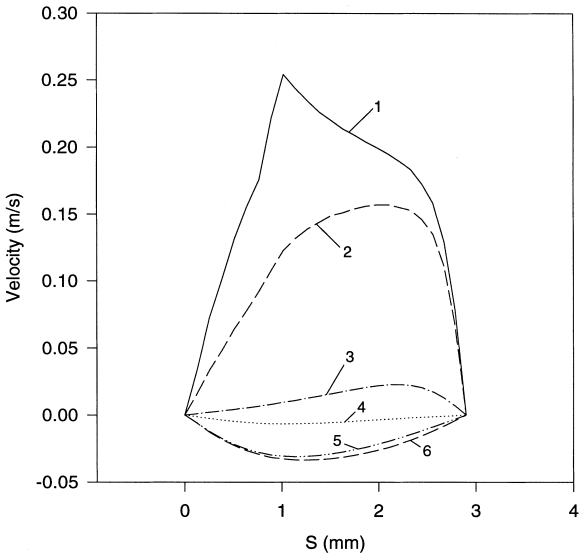

Fig. 13. Evolution of tangential velocity along the surface of the Zr droplet after the laser heating source in turned off. S is measured from the north pole to the equator. Legends: (1) $t = 0$ s; (2) $t = 0.01$ s, (3) $t = 0.2$ s; (4) $t = 0.4$ s, (5) $t = 0.6$ s; (6) $t = 0.8$ s.

5. Concluding remarks

This paper has presented a numerical study of surface deformation, thermal convection and temperature distribution in electrostatically levitated droplets. The computational methodology is based on the boundary element solution of electric potential outside the droplet, the weighted residuals formulation of the free surface balance equation involving electrostatic stresses and surface tension, and the finite element solution of the internal fluid flow and temperature distribution in the electrostatically deformed droplets. Computer programs were developed and were checked against available solutions. The results show that the droplet deforms into an ellipsoidal shape under the action of electrostatic normal stresses induced by the applied electric field in microgravity and into a blob shape with the pointy side of the surface pointing upward in normal gravity. Internal thermal convection is induced by the temperature gradient caused by non-uniform heating. The flow is primarily attributed to surface tension forces and buoyancy effects are negligible. For the cases studied, a larger temperature gradient is found in the droplets with a higher melting point, which leads to a stronger internal recirculation. The internal convection can be substantially reduced when a more uniform heating source is applied. Both temperature and fluid flow fields evolve drastically soon after the laser beam is switched off to cool the droplets into an undercooled region. The temperature gradient along the surface changes its sign as cooling continues, which in turn causes the direction of the rotating, recirculating loop in the droplet to reverse. To realize a quiescent levitation associated with electrostatic systems, careful design of the heating source is necessary to minimize the temperature difference and thus the Marangoni convection in the droplets.

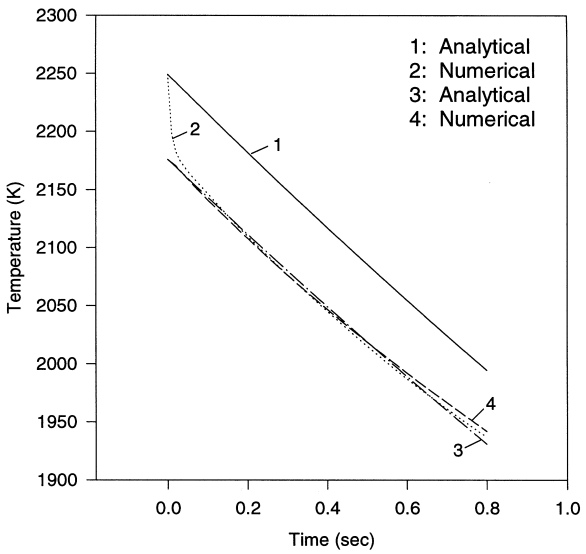

Fig. 14. Decaying of temperatures at two points (1, 2: $r = 0, z = 1.967$ mm; 3, 4: $r = 1.72$ mm and $z = 0$) on the surface of the droplet predicted by the numerical solution vs. that by a simplified analytical solution.

Acknowledgements

Financial support of this work by NASA Microgravity Science and Applications Division (Grant No. NAG8-1477) is gratefully acknowledged. Appreciation is also extended to Mr. Paul Dailey for assistance with plotting some of the computed results.

References

[1] W.K. Rhim, S.K. Chung, D. Barber, K.F. Man, G. Gutt, A. Rulison, An electrostatic levitator for high-temperature containerless materials processing in 1-g, Rev. Sci. Instrum 64 (10) (1993) 2961–2965.
[2] W.K. Rhim, Thermophysical property measurements of molten semiconductors, in: Microgravity Materials Science Conference, Huntsville, AL, USA, 1997, pp. 427–433.
[3] W.K. Rhim, Private communication, Jet Propulsion Laboratory, California Institute of Technology, Pasadena, CA, USA, 1997.
[4] G.I. Taylor, Studies in electrodynamics, Proc. R. Soc. Lond A 291 (1966) 159–171.
[5] S. Torza, R.G. Cox, S.G. Mason, Electrohydrodynamic deformation and burst of liquid drops, Phil. Trans. R. Soc. Lond A 269 (1971) 295.
[6] O.O. Ajayi, A note on Taylor's electrohydrodynamic theory, Proc. R. Soc. Lond A 364 (1978) 499–505.
[7] S.P. Song, B.Q. Li, Coupled boundary/finite element analysis of magnetic levitation processes: free surface deformation and thermal phenomena, ASME Journal of Heat Transfer 120 (1998) 492–503.
[8] F. Shen, J.M. Khodadadi, M.C. Woods, B.Q. Li, ASME Journal of Heat Transfer 119 (1997) 210–220.
[9] J-H. Zong, B.Q. Li, J. Szekely, J-H. Zong, B.Q. Li, J. Szekely, The electrodynamic and hydrodynamic phenomena in magnetically levitated droplets, Part I. Steady state behavior, Acta Astronautica 26 (6) (1992) 435–444.
[10] J-H. Zong, B.Q. Li, J. Szekely, The electrodynamic and hydrodynamic phenomena in magnetically levitated droplets, Part II. Transient behavior and heat transfer considerations, Acta Astronautica 29 (4) (1993) 305–309.
[11] B.Q. Li, The fluid flow aspects of electromagnetic levitation processes, Int. J. Eng. Sci 32 (8) (1994) 45–66.
[12] B.Q. Li, Magnetothermal phenomena in electromagnetic levitation processes, Int. J. Eng. Sci 32 (1) (1994) 1315–1336.
[13] P.M. Adornato, R.A. Brown, Shape and stability of

electrostatically levitated drops, Proc. R. Soc. Lond A 389 (1983) 101–122.
[14] J.Q. Feng, K.V. Beard, Small-amplitude oscillations of electrostatically levitated drops, Proc. R. Soc. Lond A 430 (1990) 133–154.
[15] J.D. Jackson, Classical Electrodynamics, 2nd ed., Wiley, New York, 1975.
[16] B.N. Antar, V.S. Nuotia-Antar, Fundamentals of Low Gravity Fluid Dynamics and Heat Transfer, CRC Press, Boca Raton, FL, 1993.
[17] S.P. Song, B.Q. Li, Coupled boundary and finite element computation of magnetically levitated droplet shapes, in: J.I. Frankel (Ed.), Boundary Element Technology, vol. XII, Computational Publications, Southampton, UK, 1977, pp. 239–249.
[18] S.P. Song, B.Q. Li, J.M. Khodadadi, Coupled boundary/finite element solution of magnetothermal problems, Int. J. Num. Meth. Heat and Fluid Flow 8 (3) (1998) 321–345.
[19] S.P. Song, B.Q. Li, Coupled boundary/finite element solution of magnetothermal problems, Int. J. Num. Meth. Eng 44 (1999) 1055–1077.
[20] B.Q. Li, J.W. Evans, Boundary element solution of heat convection problems, J. Comp. Phys 93 (2) (1991) 255–272.
[21] B. Pan, B.Q. Li, H.C. de Groh, Finite element analyses of magnetic damping effects on g-jitter induced fluid flow, in: J. Sygusch (Ed.), Spacebound-97, Canadian Space Agency, Montreal, Canada, 1997, pp. 347–360.
[22] J.W.S. Rayleigh, On the equilibrium of liquid conducting mass charged with electricity, Phil. Mag 14 (1882) 184–186.
[23] C.J. Smithells, Metals Reference Book, 5th ed., Butterworths, London, 1976.
[24] G.K. Bechalor, Introduction to Fluid Dynamics, Cambridge University Press, London, 1966.
[25] B.Q. Li, S.P. Song, Thermal and fluid flow aspects of electrostatic and magnetic levitation: a comparative modeling study, J. Microgravity Sci. Tech XI (4) (1998) 134–143.